Source characteristics of the Mw 6 Mutatá earthquake, Murindo seismic cluster, northwestern Colombia

Tary, Jean-Baptiste; Mojica Boada, Manuel Jose; Vargas, Carlos Alberto; Montaña Monoga, Ana Maria; Naranjo-Hernandez, David F.; Quiroga, David Ernesto

DOI
10.1016/j.jsames.2022.103728

Publication date
2022

Document Version
Final published version

Published in
Journal of South American Earth Sciences

Citation (APA)
Tary, J.-B., Mojica Boada, M. J., Vargas, C. A., Montaña Monoga, A. M., Naranjo-Hernandez, D. F., & Quiroga, D. E. (2022). Source characteristics of the Mw 6 Mutatá earthquake, Murindo seismic cluster, northwestern Colombia. *Journal of South American Earth Sciences*, *115*, 1-10. Article 103728. https://doi.org/10.1016/j.jsames.2022.103728

Journal of South American Earth Sciences 115 (2022) 103728

Contents lists available at ScienceDirect

Journal of South American Earth Sciences

journal homepage: www.elsevier.com/locate/jsames

Source characteristics of the M_w 6 Mutatá earthquake, Murindo seismic cluster, northwestern Colombia

Jean Baptiste Tary [a,*], Manuel Jose Mojica Boada [a], Carlos Alberto Vargas [b], Ana Maria Montaña Monoga [a], David F. Naranjo-Hernandez [c], David Ernesto Quiroga [d]

[a] Departamento de Geociencias, Universidad de Los Andes, Bogotá, Colombia
[b] Departamento de Geociencias, Universidad Nacional de Colombia, Bogotá, Colombia
[c] Department of Geoscience and Engineering, Delft University of Technology, Delft, the Netherlands
[d] Department of Physics, University of Alberta, Edmonton, Alberta, Canada

ARTICLE INFO

Keywords:
Moment tensor
Kinematic source inversion
Regional data
Mutatá
Colombia

ABSTRACT

The Mutatá earthquake is a M_w 6 earthquake which occurred in northwestern Colombia on September 14, 2016. This region is located at the junction between three tectonic plates, namely the South American, Nazca and Caribbean plates, and the Chocó-Panamá and Northern Andes Blocks. This event took place in the Murindo seismic zone, a zone characterized by a high seismic activity involving the Uramita fault zone, which defines the contact between the two blocks. In this study, we relocate the mainshock – aftershocks sequence and analyze the source characteristics of the Mutatá earthquake. Using data from the Colombian Seismological National Network, and after re-picking the 411 events, we obtain absolute locations exhibiting a NW-SE oriented cloud, with the mainshock being located 8 km away from its original location and at a depth of 17.6 km. The event cloud is situated at the intersection of three faults with different orientations, the NNW-SSE Uramita Fault, a NW-SE fault, and a NNE-SSW inferred fault. Using data coming from 8 broad-band seismographs within 300 km of the mainshock, we perform moment tensor and kinematic slip distribution inversions. The moment tensor inversion points to an event centroid at 20 km depth, with a predominantly double-couple mechanism. The fault orientations in the area, NW-SE orientation of the event cloud, and hypocenter – centroid technique, indicate that the NW-SE nodal plane likely corresponds to the fault plane giving a right-lateral strike-slip mechanism on a SW dipping plane. The rupture model estimated on this plane shows different slip patches, one being close to the mainshock centroid, and few other patches distributed around the mainshock except to the southeast where most of the aftershocks are located. The maximum slip for this model is approximately 0.16 m. The source characteristics of the 2016 Mutatá earthquake suggest then that secondary faults within the Murindo seismic zone can generate large earthquakes, potentially consisting in an important source of seismic hazard in this region.

1. Introduction

The northwestern corner of South America is characterized by the presence of three major converging plates, with the Caribbean and Nazca plates subducting beneath the South American plate, and the Chocó-Panamá block (Fig. 1). The Nazca and Caribbean plates are also divided in a number of flat and dipping segments (e.g., *Vargas and Mann, 2013*; *Cornthwaite et al., 2021*; *Sun* et al., *2022*). In the case of the Nazca plate, flat and normally dipping segments are located North and South of ~5°N, respectively. Relative to the stable South American plate, the Chocó-Panamá block (CPB) is converging eastward toward the Northern Andes Block (NAB) at a rate of ~15–18 mm/yr, while the NAB is escaping to the northeast at ~8.6 mm/yr (*Mora-Páez* et al., *2018*). The NAB is undergoing compression induced by the CBP and the subducting Caribbean plate, and right-lateral transpression due to the oblique subduction of the Nazca plate (*Taboada* et al., *2000*; *Cortés and Angelier, 2005*; *Arcila and Muñoz-Martín, 2020*).

Due to the interactions between these different plates and blocks, numerous seismically active structures are present at the limit between the CPB and the NAB, which is currently referred to as the Uramita Fault Zone (UFZ) (Fig. 1) and the Itsmina deformed zone for the northern and southern parts, respectively (*Léon* et al., *2018*). In the northern part, the

* Corresponding author. Departamento de Geociencias, Universidad de los Andes, Cra 1 #18A-12, Bloque M1, Bogotá, Colombia.
E-mail address: jb.tary@uniandes.edu.co (J.B. Tary).

https://doi.org/10.1016/j.jsames.2022.103728
Received 11 November 2021; Received in revised form 5 February 2022; Accepted 6 February 2022
Available online 16 February 2022

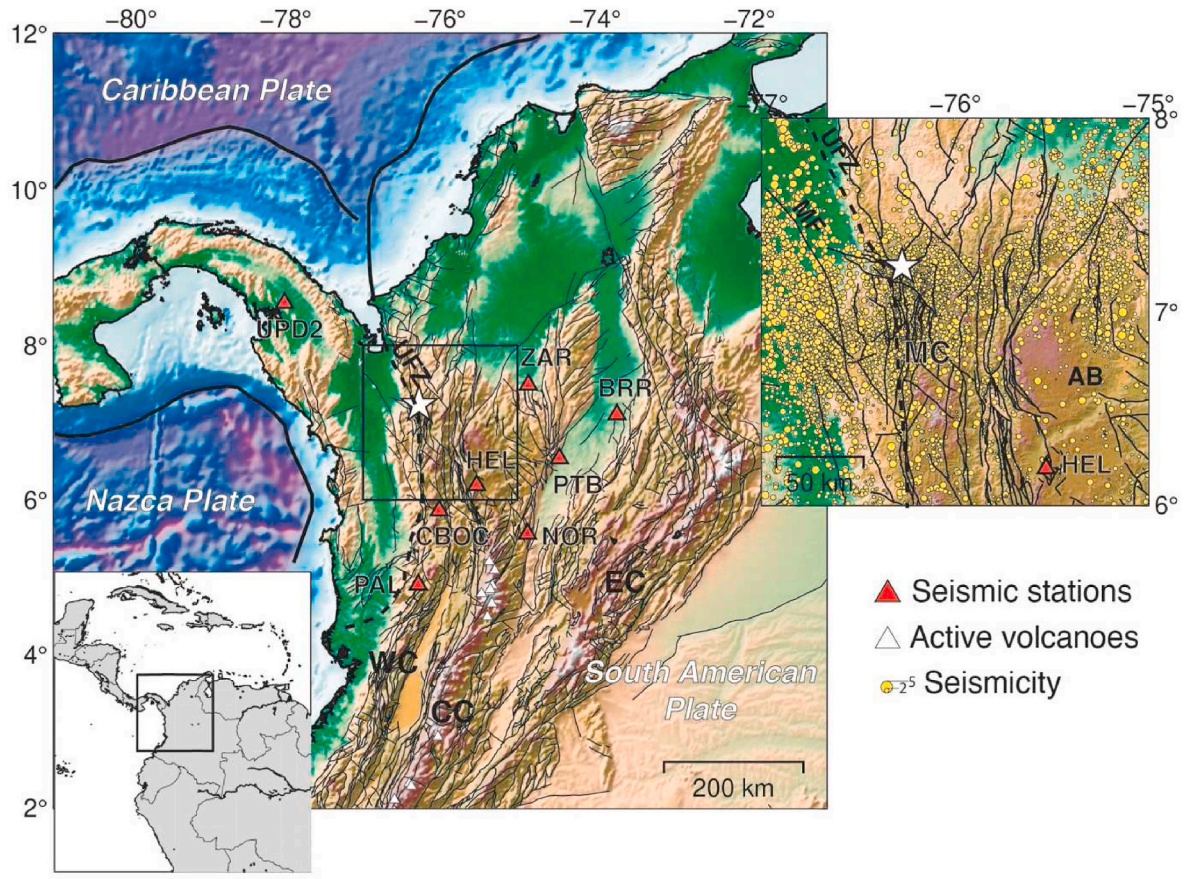

Fig. 1. Map of the northwestern part of Colombia, whose position is shown by the inset, with the faults indicated by black lines (from *Gómez et al., 2015*), active volcanoes by white triangles (Global Volcanism Program of the Smithsonian Institute), and the black square indicating the position of the enlarged map on the right. The seismological stations used for the moment tensor and slip distribution inversions are indicated by the red triangles. The Mutatá mainshock position obtained in this study is indicated by the white star. The black dashed line indicates the limit between the North Andean Block to the East and the Chocó-Panama Block to the West (*León et al., 2018*). Seismicity located by the Colombian Geological Service between 1993 and 2016 is indicated by yellow dots (symbol size scaling with their magnitude). AB: Antioquia Batholith, CC: Central Cordillera, EC: Eastern Cordillera, WC: Western Cordillera, MC: Murindo Cluster, MF: Murindo Fault, UFZ: Uramita Fault Zone.

Table 1
Reference 1D P-wave and S-wave velocity models of Vargas (2020) (depths between 0 and 40 km), completed at depth with the ak135-f model (Kennett et al., 1995; Montagner and Kennett, 1996). For the crust, a V_p/V_s ratio of 1.78 is used to calculate S-wave velocities instead of the values presented in this table.

Depth (km)	V_p (km/s)	V_s (km/s)
0	6.0	3.1
15	6.7	3.6
40	7.8	4.0
50	7.89	4.43
189	8.31	4.73

UFZ is characterized by high seismic activity, including the Murindo seismic cluster, which is the most active crustal seismic cluster in Colombia. This part of the UFZ, encompassing the Murindo seismic cluster, is squeezed between the CPB to the West and the Antioquia batholith to the East (Fig. 1). The Murindo seismic cluster is located between longitudes of 75.5°W and 78°W, and latitudes of 6°N and 8°N (*Dionicio and Sánchez, 2012*). Between 1993 and 2016, the earthquakes located by the Colombian Geological Service in this zone amount to almost 6500 events with magnitudes ranging between 0.4 and 6.4. Significant historical events in this area include the M_w 5.9 1952 Mutatá earthquake, the M_w 6.5 1977 Apartadó earthquake, the M_w 7.1 1992 Murindo seismic sequence (*Li and Toksöz, 1993*; *Arvidsson* et al., *2002*; *Dionicio and Sánchez, 2012*), and the M_w 6 2016 Mutatá earthquake.

Despite the high seismic activity and the growing information on potentially tectonically active structures in the Murindo seismic zone, the actual activity of each structure is still unclear. This study focuses on the source characteristics of the most recent large magnitude event in this region, the M_w 6 2016 Mutatá earthquake, and its aftershocks. Using a velocity model recently developed by *Vargas (2020)*, we use regional seismological data acquired by the Colombian Seismological National Network to first relocate the mainshock-aftershocks sequence, and then compute both moment tensor and finite-fault slip distribution for the Mutatá earthquake. We finally provide a discussion on possible tectonic interpretations for this event and its aftershocks, with the rupture of NW-SE oriented fault or faults, and implications for seismic hazards in this area.

2. Geological and tectonic background

The Murindo seismic zone and Mutatá earthquake are located at the limit between the CPB and NAB. The NAB comprises highly deformed oceanic and continental terranes accreted to South America at different times (*Restrepo and Toussaint, 1988*), while the CPB is constituted by different oceanic terranes which were accreted to the northwestern edge of the Western Cordillera during the Neogene (*Duque-Caro, 1990*; *Taboada, 2000*; *León* et al., *2018*; *Cardona* et al., *2018*). The indentation of the CPB is contemporary to the onset of the main Andean tectonic phase suggesting a possible relation with the deformation undergone by the NAB north of 5°N. The eastern tectonic boundary of the CPB is

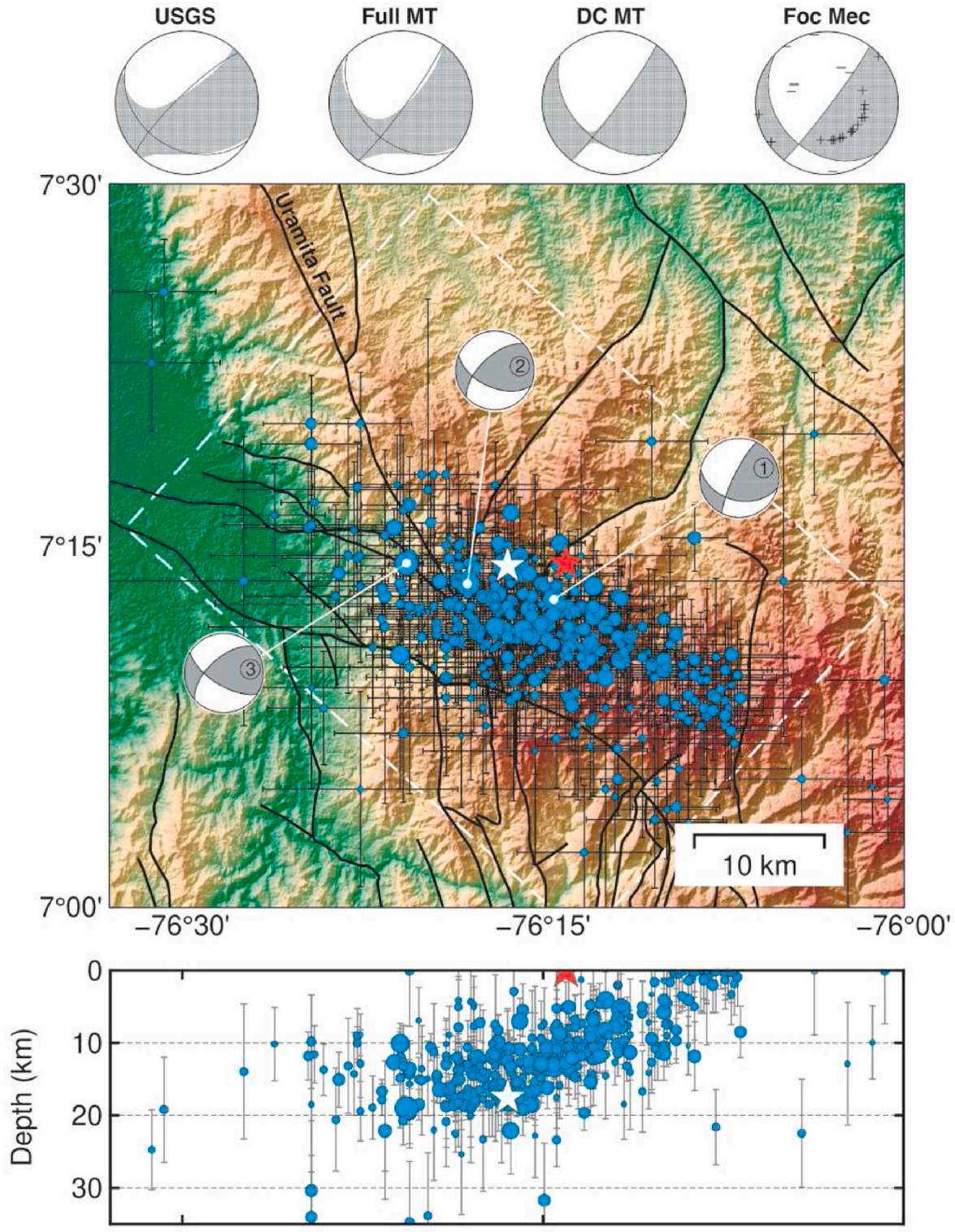

Fig. 2. Mainshock and aftershocks (blue dots) absolute locations showing events with horizontal and vertical uncertainties lower than ± 20 and ± 10 km, respectively. Black lines indicate the faults from *Gómez* et al. *(2015)*, and the white dashed rectangle corresponds to the fault plane used for the kinematic slip inversion. Above the map are shown moment tensor and focal mechanism solutions obtained in this study and by the USGS for the Mutatá earthquake. Mainshock locations from the Colombian Geological Service and determined in this study are indicated by the red and white stars, respectively. The three focal mechanisms presented on the map correspond to those of the three strongest aftershocks (1 and 3 with a M_w of 4.7 and 2 with a M_w of 4.6).

defined by the left-lateral Uramita Fault Zone (UFZ), while the Itsmina deformed zone is associated with its southern border (*Case* et al., *1971*; *Restrepo and Toussaint, 1988*; *Duque-Caro, 1990*; *Taboada* et al., *2000*). The Itsmina deformed zone consists of a 40 km wide zone of highly deformed sedimentary rocks extending for about 320 km from the Pacific coast to the eastern flank of the Western Cordillera (*Duque-Caro, 1990*). A large area of the CPB located between the Colombian coast and the UFZ also exhibits a larger strain rate compared with the surrounding

Table 2
Summary of parameters for moment tensor and kinematic slip distribution inversions. Parameters in bold correspond to those of the preferred slip distribution model.

Parameters	Values obtained/used
Origin time[a]	14/09/2016 1:58:30.30 UTC
Epicenter[a]	7.236°N, 76.275°W
Hypocenter[a] and centroid[b] depths	17.6 ± 12.6 km, 20± 3 km
Strike – dip – rake[b]	N132°E/43°/−173°
Inversion frequency band	0.03–0.09 Hz
Number of stations	8
Fault plane dimensions	50 × 50 km
Subfault size and number	~3 km × 3 km, 289
Number of time windows and overlap	5 or **10**, 50%
Rise time	1.1 s
Maximum rupture velocity	**2.5**, 2.8, 3.2 km/s

[a] Values corresponding to the absolute location in this study.
[b] Values coming from the double-couple moment tensor inversion.

areas, including Panama to the North and the NAB to the East (*Arcila and Muñoz-Martín, 2020*).

The UFZ marks the suture between the CPB and the NAB and appears as a major fault zone delineating the boundary between the turbidites in the Western Cordillera and the melange materials in the Dabeiba Arch. This tectonic contact is observed as north as the Urabá Gulf and seems to be the northernmost surface continuation of the Atrato fault (*Duque--Caro, 1990*). The occurrence of earthquakes clustered within the UFZ indicates that this fault zone is currently reactivated with a left-lateral transpressional regime (Fig. 1) (*León* et al., *2018*). The northern segment of the UFZ is often covered by middle Miocene to Pliocene sedimentary sequences leading to a poor constrain of structural data in this area (*Restrepo and Toussaint, 1988; Arvidsson* et al., *2002; León* et al., *2018*). Although the nature of the CPB-NAB suture is still unclear, the recent seismicity seems to support the existence of a diffuse deformation zone instead of a sharp border (*Arvidsson* et al., *2002*; *Cardona* et al., *2005*).

In the area corresponding to the 2016 M_w 6 Mutatá earthquake and the Murindo seismic cluster, the main faults of the UFZ change orientation from a more NW-SE to a NNW-SSE to N–S direction (Fig. 1) (*Gómez et al., 2020*). In addition to these main structures, including the Uramita and Murindó faults, smaller faults are also present with orientations varying from WNW-ESE to NW-SE such as the Cañasgordas fault (*Gómez et al., 2020*). Alternatively, *París* et al. *(2000)*, mention the Murindó, Murri and Mutatá faults in this area of the UFZ. The Murindó Fault, which is located along the western flank of the Western Cordillera, is a left-lateral or right-lateral fault depending on the segment (*Gómez et al., 2020*). This fault has been associated with a M_w 7.2 earthquake, which occurred in this region in 1992, and its seismic activity has been recorded since 1883 (*París* et al., *2000*; *Cardona* et al., *2005*; *Arias* et al., *2009*). According to *París* et al. *(2000)*, the fault has an average strike of N12.6°W with a probable dip to the East. However, the concentration of a significant part of the aftershocks associated with the M_w 7.2 event to the West of the Murindó fault surface trace suggests that the fault might be dipping in this direction instead (*Arias* et al., *2009*; *Dionicio and Sánchez, 2012*). The Murri fault has a reverse dextral movement and is located to the South of the Mutatá earthquake and its aftershocks (*Gómez et al., 2020*).

3. Methods

3.1. Velocity model

In this study, we use a 1D crustal velocity model based on the 3D tomography velocity model computed by *Vargas (2020)*. This model was computed using arrival times of P and S phases observed at 113,269 local earthquakes recorded by 33 seismological stations of the Colombian Seismological National Network. Only initial hypocentral solutions calculated using at least six stations were considered and both P and S phases were carefully handpicked. The definition of the 3D velocity structure started with a 1D model (*Ojeda and Havskov, 2001*) for inverting new hypocentral locations with HYPOCENTER (*Lienert and Havskov, 1995*). In depth, velocities were linearly interpolated between layers to define the reference starting model for the 3D inversion.

The 3D velocity model was then estimated using a subset of >14,000 well-located earthquakes and the LOTOS algorithm for local earthquake tomography (*Koulakov, 2009*). It performs iterative simultaneous inversions for P and S velocities and source parameters, using an adaptive mesh parameterization with nodes distributed inside the study volume and guaranteeing no nodes in areas with a deficit of ray coverage (less than 10% of average ray density). The criteria for selecting the subset of events included: (1) earthquakes located within the seismic network, and (2) the spatial distribution of the events guaranteeing as uniform a sampling as possible in the study area. In the following, we carry out the event absolute locations, source parameter estimations and slip inversion, with the 1D reference velocity model of this 3D velocity model. Since this 1D velocity model only includes the crustal part (i.e., depths <40 km), we completed the deeper part with the ak135-f model (Table 1) (*Kennett* et al., *1995*; *Montagner and Kennett, 1996*).

3.2. Earthquake sequence absolute locations

The Mutatá sequence including the mainshock and its aftershocks were originally processed by the Colombian Seismological National Network of the Colombian Geological Service (SGC), corresponding to 411 events in total. These aftershocks have local magnitudes ranging between 0.7 and 4.5, forming a NW-SE oriented cloud (Fig. 2). After recovering the individual files, we manually revised the events leading to a total of 3557 P-wave picks and 3246 S-wave picks. We then employed the probabilistic, non-linear location algorithm NonLinLoc (*Lomax et al., 2009*) to locate the events. Information on station positions, velocity model, picking times, and trial event locations are combined into an *a posteriori* probability density function (*Lomax et al., 2009*). Travel-time tables are computed for all trial locations on a grid using a finite-difference implementation of the Eikonal equation (*Podvin and Lecomte, 1991*). In the present case, we employ the equal-differential time likelihood function and the oct-tree search algorithm to reach the optimal solution. The events are located using the 1D-reference P-wave velocity model described in the previous section, with a V_p/V_s of 1.78 determined using test locations and their root-mean-square residuals. Picking time uncertainties between 0.1 and 2 s were attributed to P- and S-wave picks depending on pick quality. Finally, only events with at least six phase-time picks for stations within a radius of 500 km from the event absolute locations were included in the location.

3.3. Centroid moment tensor calculation

The W-phase moment tensor estimated by the USGS presents a large non-double-couple (DC) component (45%) (Fig. 2). This large non-DC component cannot be explained using the limited information available for this area (e.g., presence of fluids). We then assess the necessity of this component in the moment tensor solution using regional stations operated by the Colombian Geological Service and the same 1D velocity model. We selected eight broad-band seismological stations (i.e., frequency range 120 s to 50 Hz, with instruments Reftek RT151, Streckeisen STS-2.5, Güralp CMG-3ESP, and Nanometrics Trillium Compact) distributed around the mainshock based on their distance to the event (<300 km) and their data quality (Fig. 1). The mainshock epicenter is set at the location obtained with NonLinLoc, with a depth allowed to vary between 5 and 35 km by increments of 1 km.

To calculate the moment tensor, we use the ISOLA software suite of *Sokos and Zahradnik (2008)*, and *Sokos and Zahradnik (2013)*. The 3-component seismograms are first pre-processed, including mainly decimation, band-pass filtering, and the instrument's response removal.

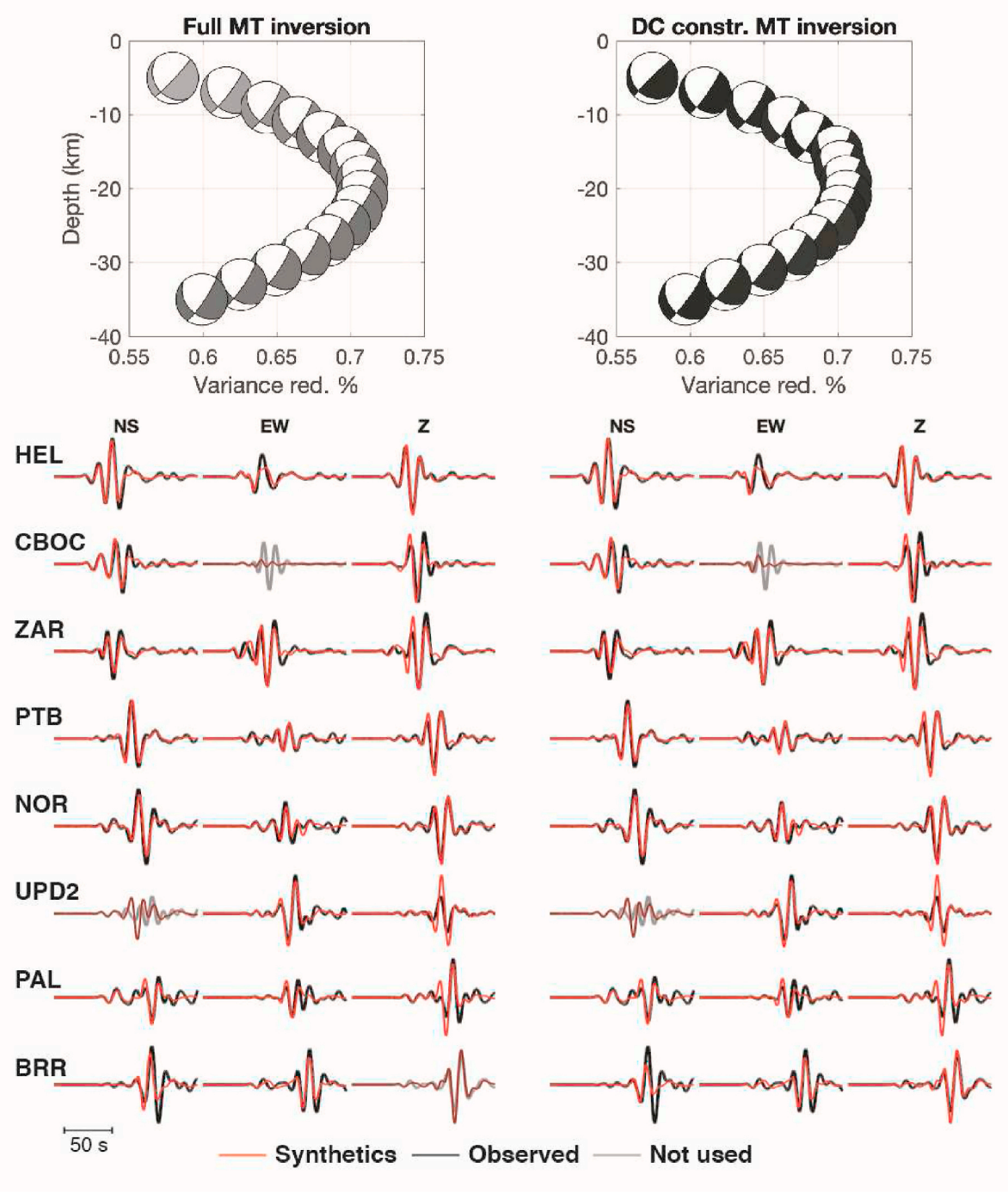

Fig. 3. Changes in moment tensor solutions and variance reduction with mainshock depth for the full moment tensor and DC-constrained tensor inversions. The gray intensity of moment tensor solutions indicates their DC component percentage (white: 0%, black: 100%). Waveforms correspond to synthetics and observed data after processing for the solutions with highest variance reductions (depth of 20 km), filtered between 0.03 and 0.09 Hz.

Assuming a point source, Green's functions are then calculated for a set of trial sources and the different stations using the discrete wavenumber technique (*Bouchon, 1981*). The optimal moment tensor is then obtained through a least-squares inversion for different origin times and the previously defined point source locations.

The full moment tensor, as well as deviatoric and double-couple moment tensors, can be computed. The main parameter to determine is the frequency band used in the inversion. Here we use a frequency band between 0.03 and 0.09 Hz, defined after examining the signal-to-noise ratio of the selected stations and the solution stability. The solution quality is then assessed comparing the different solutions available (i.e., USGS, focal mechanism, moment tensors calculated in this study), the variance reduction (VR) corresponding to the fit between synthetics and observed waveforms, the condition number (CN) of the Green's function matrix, the focal-mechanism variability index (FMVAR) and the space-time variability index (STVAR) (*Sokos and Zahradník, 2013*).

3.4. Kinematic slip distribution inversion

Using the same general parameters as those determined for the moment tensor inversion (i.e., frequency band, selected stations, velocity model), we performed a kinematic slip distribution inversion of

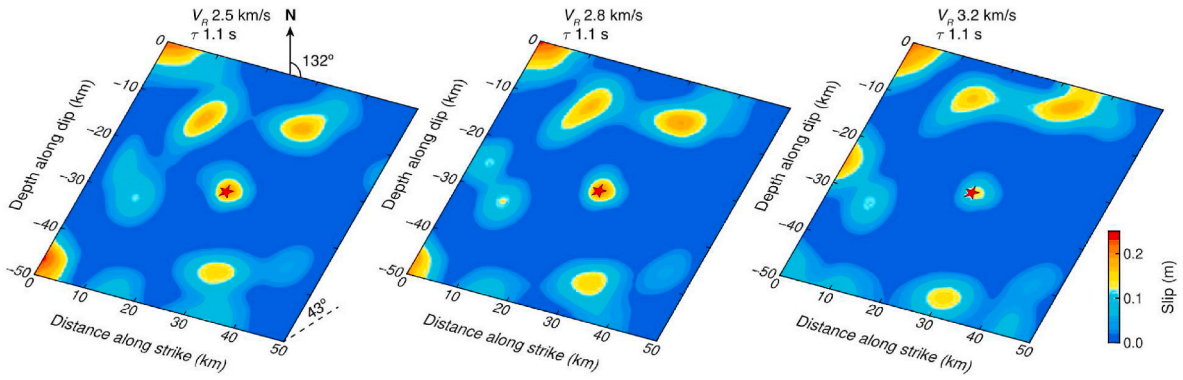

Fig. 4. Slip distributions obtained for three kinematic slip distribution inversions using three different maximum rupture velocities and the parameters presented in Table 2. The red star corresponds to the mainshock centroid position.

the regional seismological data to determine the rupture process of the Mutatá earthquake. The same main pre-processing steps are applied to the seismological data using ObsPy (*Beyreuther et al., 2010*), including decimation, band-pass filtering and instrument's response removal. The kinematic slip inversion is carried out using the multi-time window method (e.g., *Hartzell and Heaton, 1983*; *Ide, 2007*) together with the non-negative least-squares (*Ide, 2007*).

Here we use the MudPy code to carry out the kinematic slip distribution inversion (e.g., *Melgar et al., 2015*). This kind of method, discretizing the rupture in both time and space, is commonly used to study the rupture process of moderate to large earthquakes (e.g., *Chi et al., 2001*; *Melgar et al., 2015*). In time, the rupture is divided into overlapping triangular source time functions whose durations are defined by the rise time (Table 2). In space, we use a fault plane with dimensions of 50 by 50 km, as well as a strike and dip given by the general aftershock cloud orientation and the corresponding plane of the focal mechanisms and moment tensors. We further discretize the fault plane into smaller $\sim 3 \times 3$ km subfaults summing up to 289 subfaults in total. For each pair source-subfault, Green's functions are computed using the frequency-wavenumber technique implemented by *Zhu and Rivera (2002)*. This kind of inversion being an ill-posed problem, spatial and temporal smoothing is introduced. The amount of smoothing is indicated by the Akaike Bayesian Information Criterion (ABIC) (*Melgar et al., 2015*). The final selection of optimal slip distribution models is based on the smoothing (i.e, ABIC), VR, moment magnitude, rise time and maximum rupture velocity V_R. All these essential parameters and others are listed in Table 2.

4. Results

4.1. Absolute locations and moment tensors

A total of 410 events were located using the aforementioned procedure, with only one event having less than six phases (Fig. 2). These absolute locations have an average root-mean square residual in traveltime of 0.31 s. The horizontal uncertainties range mainly between 2 and 20 km, while vertical uncertainties range mainly between 3 and 20 km. The M_w 6 mainshock epicenter location shifts to the West by ~8 km relative to the original epicenter provided by the SGC, with new coordinates and depth corresponding to 7.236°N, 76.275°W and 17.6 km. Horizontal and vertical uncertainties are estimated at 5.6 and 12.6 km, respectively. The aftershocks form an elongated cloud in the NW-SE direction, with most event depths being similar or lower than the one of the mainshock.

Two moment tensors were calculated using the eight selected stations presented in Fig. 1. First, the full moment tensor is calculated using a frequency band of 0.03–0.09 Hz for all stations. The centroid moment tensor obtained in this case is very similar to the one estimated by the USGS (Fig. 2), with a non-DC component of 39%. The total VR reaches a maximum of 70.8% when the centroid is at a depth of 20 km. Trial sources between 17 and 24 km all show VR > 70% and very similar solutions (Fig. 3), which provides an estimation of the uncertainty in depth for this event. Other quality assessment measures include a CN of 5.5, FMVAR 16 ± 24, and STVAR 0.10, all indicating a well-constrained solution (*Sokos and Zahradník, 2013*). In order to test the importance of having the non-DC part within the moment tensor solution and its impact on the solution quality, we also calculated the double-couple moment tensor (i.e., DC-constrained) with the same parameters (e.g., same stations and frequency band). In this case, the total VR reaches a maximum of 70.6% at a depth of 20 km. As for the full-MT solution, similar solutions and VR larger than 70% are obtained for depths between 17 and 23 km (Fig. 3). For this solution, the non-DC part represents only 5.7%, the CN is 2.1, the FMVAR 9 ± 5, and the STVAR 0.09. All quality measures also correspond to a well-constrained solution.

Comparing both centroid moment tensor solutions, the similarity in VR and solution quality indicates that including a non-DC part doesn't significantly improve the solution. Its presence within the solution is then not necessary to better explain the seismological data. To further compare the nodal plane positions, a focal mechanism was also calculated based on P-wave first motion polarities with the SEISAN implementation of FOCMEC (*Snoke* et al., *2003*; *Havskov and Ottemöller, 1999*). All moment tensor solutions as well as the focal mechanism have very consistent nodal plane orientations, with the DC-constrained moment tensor having one plane oriented NW-SE (N132°E) and dipping at 43° toward the southeast, and the other being near-vertical and oriented NE-SW (N36°E) (Fig. 2). Focal mechanisms calculated for the three strongest aftershocks having magnitudes between M_w 4.6 and 4.7 show relatively similar solutions with one nodal plane being oriented NW-SE and the other oriented NE-SW. Lower magnitude aftershocks with local magnitudes between 3.5 and 4.5 also present similar polarity distributions, which suggests they have similar focal mechanism solutions.

4.2. Kinematic slip distribution inversion

In order to determine which nodal plane is the fault plane and its orientation for the slip inversion, we combined the information provided by the local structural information, the aftershock cloud orientation, the focal mechanisms and the Hypocenter-Centroid configuration (H–C plot, *Zahradnik et al., 2008a*). The mainshock and its aftershocks are located at the intersection of the southern end of the Uramita fault which, in this zone, has a strike of N25-30°W, NW-SE oriented faults with strikes between around N115°E and N135°E, and a NE-SW inferred fault oriented at N25-30°E (Fig. 2) (*Gómez et al., 2020*). Both structural and seismological information suggest then that the NW-SE oriented nodal plane corresponds to the fault plane. The DC moment tensor and focal

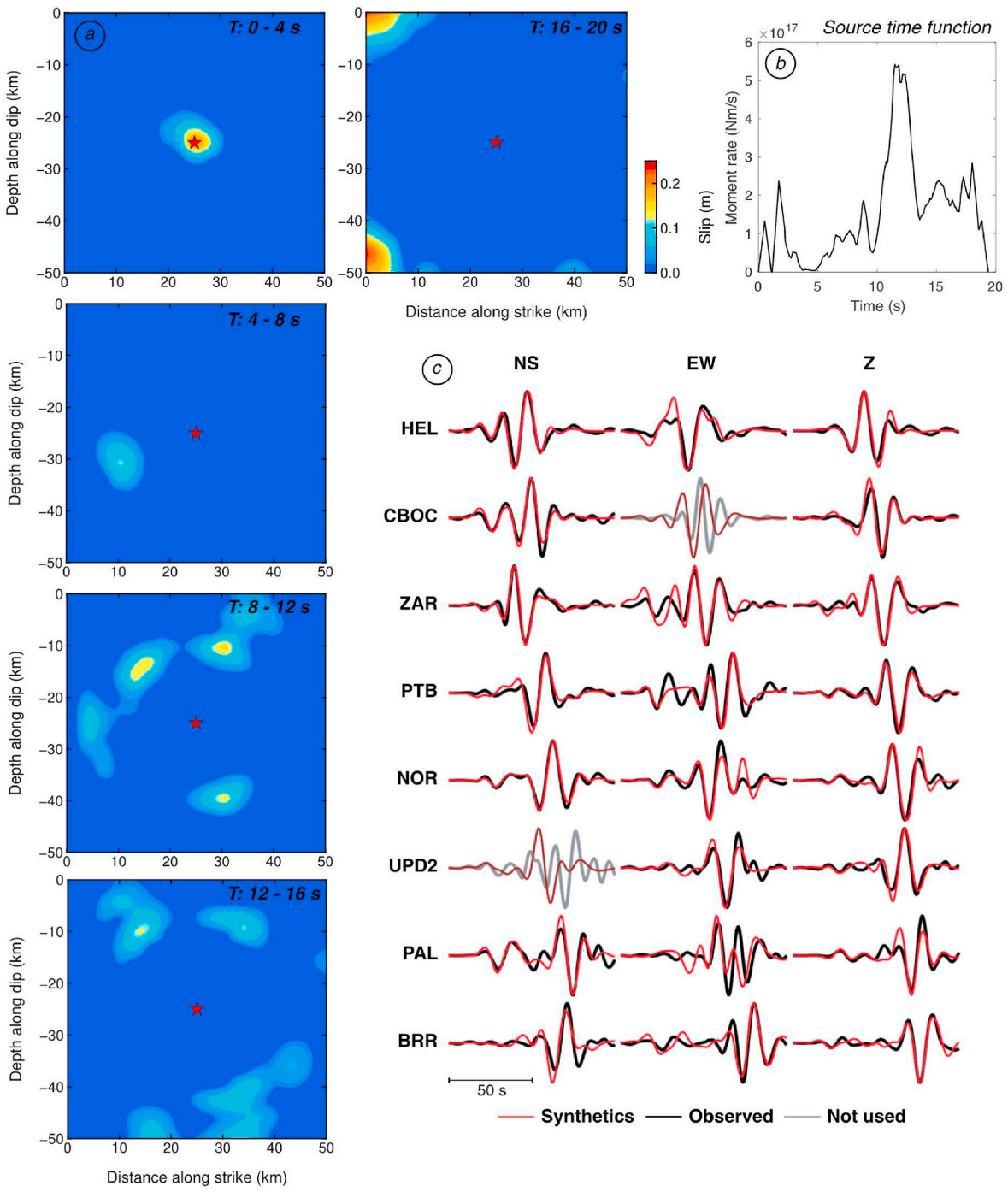

Fig. 5. Rupture process (a), source time function (b), and synthetics and observed waveforms after processing (c) (filtered between 0.03 and 0.09 Hz), corresponding to the kinematic slip distribution inversion using a rupture velocity of 2.5 km/s, a rise time of 1.1 s, and other parameters listed in Table 2.

mechanism of the Mutatá earthquake show then a mainly right-lateral strike-slip mechanism. Most of the aftershocks would be located in the hanging wall of the main event.

To invert for the slip distribution, we defined a fault plane with the centroid at its center, sides of 50 km and subdivided into approximately 3 by 3 km subfaults. Many inversions were carried out to evaluate the influence of some parameters on the results, namely the maximum rupture velocity, rise time, number of time windows, and smoothing parameters. The maximum rupture velocity is generally within 0.65 β and 0.85 β, with β the S-wave velocity at the hypocenter position (Heaton, 1990). Using a S-wave velocity of ~3.8 km/s we obtain a range of rupture velocities between ~2.5 and 3.2 km/s. We then use three different maximum rupture velocities 2.5, 2.8 and 3.2 km/s. The rise time is then estimated using the subfault dimensions and rupture velocities as L/V_R (i.e., $0.9 < \tau < 1.2$ s), where L is the subfault length. For the number of time windows, the values of 5 and 10 were selected.

With five time windows, none of the slip distribution models reaches a VR of 80%. In the following, we will then focus on the results using ten time windows. Comparing the results using a rise time of 1.1 s and the three different maximum rupture velocities, the VR ranges between 76.9 and 80.1% with a maximum for the maximum rupture velocity of 2.5 km/s (Fig. 4). For all these models the fit between synthetic and observed waveforms is very high (Fig. 5). The slip distributions obtained using these three maximum rupture velocities are also similar, showing

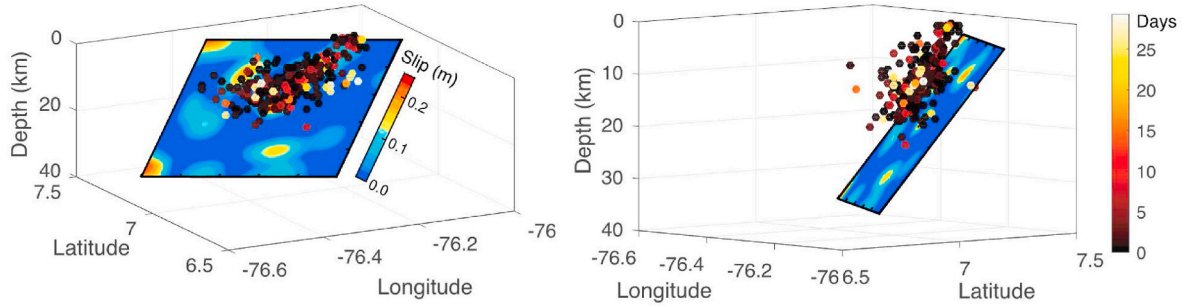

Fig. 6. Three-dimensional configuration of the fault plane with the coseismic slip distribution ($V_R = 2.5$ km/s, $\tau = 1.1$ s) and the aftershock distribution. The aftershocks are color-coded by their occurrence time after the mainshock.

several main patches on the fault plane (Fig. 4). One of these patches is located close to the centroid location, two are located closer to the shallow part of the fault plane, one is located to the northwest of the centroid, and another one is located deeper, to the south of the centroid. Focusing on the model with the highest VR (i.e., maximum $V_R = 2.5$ km/s, $\tau = 1.1$ s), the average and maximum slip estimated for the Mutatá earthquake are around 0.03 and 0.16 m, respectively. The total seismic moment corresponding to this model is around 3×10^{18} N m, corresponding to a moment magnitude of 6.25. For a total duration of around 19 s, the source time function shows a small peak between 0 and 4 s, followed by one main peak between 9.5 and 13.5 s and a roughly constant moment rate for ~6 s (Fig. 5). The rupture started close to the mainshock position, followed by a small patch to the northwest of the mainshock (Fig. 5). The rupture then propagated in all directions around the mainshock except to the southeast. The rupture finally ended in the upper and lower corners to the northwest of the mainshock.

5. Discussion

The contact between the CPB and the NAB in the Murindo seismic zone, corresponding to the Uramita fault zone, is characterized by a high seismic activity. An important part of this seismicity is however difficult to assign to specific structures mainly due to event location uncertainties, limited information on their source attributes (e.g., focal mechanisms), the high number of seismogenic structures, and the potential presence of unknown faults or faults with unclear/varying characteristics in the area. In this context, and despite the information brought by the aftershock alignment, focal mechanisms and moment tensor solutions, significant uncertainties remain on the definition of source characteristics (e.g., fault plane for the finite fault slip inversion) and tectonic interpretations. For the 2016 Mutatá earthquake, the aftershock number decreases exponentially over time, with more than 50% of the aftershocks occurring within one day of the mainshock. In addition, the aftershocks are immediately triggered in all parts of the event cloud (Fig. 6). Hence, their spatio-temporal pattern does not present a diffusion-like distribution, which could indicate the presence of fluids and explain the large non-DC components in full moment tensor inversions (e.g., *Julian et al., 1998*). The presence of valid non-DC components can also arise due to rupture complexity (e.g., *Zahradnik et al., 2008b*) or rock anisotropy (*Vavryčuk, 2005*), for example. In our case however, for the W-phase USGS and full moment tensors, it likely corresponds to spurious components due to the use of a 1D velocity model, observational limitations (data coverage and quality, centroid location), and modelling limitations (frequency band, overfitting) (e.g., *Duputel et al., 2012*). This then illustrates the importance of regional studies to re-examine earthquake source characteristics.

Structural information and our seismological results suggest that the fault plane corresponds to the nodal plane oriented NW-SE, corresponding to a right-lateral strike-slip mechanism. This focal mechanism is roughly in agreement with the general NW-SE compressional stress regime in this area (*Arcila and Muñoz-Martín, 2020*). The main structures in this zone, such as the Uramita, Murindo and Cañasgordas faults, show mainly a left-lateral strike-slip regime (e.g., *París* et al., *2000*; *Gómez et al., 2020*). However, the Murindo seismic zone presents a variety of focal mechanisms, generally showing a strike-slip component, sometimes combined with either normal or reverse components in different amounts (*Cardona* et al., *2005*; *León* et al., *2018*; *Castillo Manrique, 2018*). This suggests that this zone is accommodating the deformation between the CPB, NAB and Antioquia batholith by means of complex interactions between different faults. Within the mainly left-lateral strike-slip Uramita fault zone, a NW-SE oriented antithetic fault could have generated the 2016 Mutatá earthquake.

The slip distribution results indicate that the rupture occurred in most directions except to the southeast (Figs. 4 and 6). Most aftershocks being located in this direction (Figs. 2 and 6) and, considering location uncertainties, this suggests that stress changes due to the mainshock triggered seismicity either on another part of the same fault plane, or on shallower structures in the hanging wall of the mainshock. Tectonic interpretations remain however speculative considering the uncertainties associated with the fault plane definition. On the other hand, characterizing the source of significant events, such as the Mutatá earthquake, provides important information on the seismic activity and the seismogenic potential of the various tectonic structures present in the northwestern part of Colombia.

6. Conclusion

Located at the contact between CPB and NAB, the Uramita fault zone includes the Murindo seismic zone presenting high seismic activity in terms of numbers and magnitudes. The M_w 6 2016 Mutatá earthquake, which occurred within this zone, is situated at the intersection of the Uramita fault with NW-SE-oriented faults and a NNE-SSW-oriented inferred fault. After relocation, the earthquake sequence, comprising the mainshock and its aftershocks (i.e., 410 events), make a NW-SE-oriented cloud with most of the aftershocks being located above and to the southeast of the mainshock. A re-analysis of its source mechanism using eight regional seismological stations points to a DC moment tensor, an event centroid at a depth of 20 km, and a right-lateral mechanism for a NW-SE fault plane dipping toward the southwest. Considering the main kinematic slip distribution inversion parameters (i.e., smoothing, number of time windows, rise time, maximum rupture velocity), the maximum variance reduction is obtained for a rise time of 1.1 s and maximum rupture velocity of 2.5 km/s. The corresponding rupture model has a source time function of about 19 s and slip patches distributed around the mainshock centroid location in all directions except to the southeast, where most of the aftershocks are located. The Murindo seismic zone shows a variety of focal mechanisms likely reflecting complex interactions between faults within a regional NW-SE compressional regime. The source characteristics of the M_w 6 2016 Mutatá earthquake suggests then that secondary faults are capable of generating large magnitude earthquakes, and hence contribute substantially to seismic hazard in this region.

Data availability

The regional seismological data used in this study are available on the Servicio Geológico Colombiano webpage http://bdrsnc.sgc.gov.co/paginas1/catalogo/index.php. The Jupyter Notebook using ObsPy and MudPy to pre-process seismological data and calculate the kinematic slip inversion of the Mutatá earthquake is available at https://github.com/jbtary.

CRediT authorship contribution statement

Jean Baptiste Tary: Writing – original draft, Supervision, Software, Methodology, Investigation, Funding acquisition, Formal analysis. **Manuel Jose Mojica Boada:** Writing – original draft, Software, Investigation, Formal analysis. **Carlos Alberto Vargas:** Writing – original draft, Investigation. **Ana Maria Montaña Monoga:** Investigation, Formal analysis. **David F. Naranjo-Hernandez:** Writing – review & editing, Software, Investigation. **David Ernesto Quiroga:** Writing – review & editing, Software, Investigation.

Declaration of competing interest

The authors declare that they have no known competing financial interests or personal relationships that could have appeared to influence the work reported in this paper.

Acknowledgments

We thank the Red Sismológica Nacional de Colombia of the Servicio Geologico Colombiano for the access to the seismological data presented in this study, and the semillero of Seismology of Colombia of the Universidad de los Andes for helping with the picks revision of the 2016 Mutatá sequence. We also thank the Editor and an anonymous reviewer for their valuable comments. J. B. T. acknowledges funding from the Universidad de los Andes (FAPA project: PR.3.2016.3047) and the Fundación para la Promoción de la Investigación y Tecnología of the Banco de la República (project: 4.556). C. A. V. thanks the Universidad Nacional de Colombia, Department of Geosciences for the partial support to this research (project HERMES 10691), and the MINCIENCIAS (project 110185271555). The Generic Mapping Tool (GMT) was used for some of the figures of this article.

References

Arcila, M., Muñoz-Martín, A., 2020. Integrated perspective of the present–day stress and strain regime in Colombia from analysis of earthquake focal mechanisms and geodetic data. In: Gómez, J., Pinilla–Pachon, A.O. (Eds.), The Geology of Colombia, Volume 4 Quaternary, vol. 38. Servicio Geológico Colombiano, Publicaciones Geológicas Especiales, Bogotá, pp. 549–569.

Arias, J.P.M., Muñoz, L.Y.V., Cardona, L.M.R., 2009. Analisis macrosismico del terremoto de murindo-antioquia (Colombia) octubre de 1992. Bol. Geol. 31 (1).

Arvidsson, R., Boutet, J.T., Kulhanek, O., 2002. Foreshocks and aftershocks of the Mw = 7.1, 1992, earthquake in the Atrato region, Colombia. J. Seismol. 6 (1), 1–11.

Beyreuther, M., Barsch, R., Krischer, L., Megies, T., Behr, Y., Wassermann, J., 2010. ObsPy: a Python toolbox for seismology. Seismol Res. Lett. 81 (3), 530–533.

Bouchon, M., 1981. A simple method to calculate Green's functions for elastic layered media. Bull. Seismol. Soc. Am. 71 (4), 959–971.

Cardona, C., Salcedo, E.D.J., Mora, H., 2005. Caracterización sismotectónica y geodinámica de la fuente sismogénica de Murindó-Colombia. Bol. Geol. 27 (1), 115–132.

Cardona, A., León, S., Jaramillo, J.S., Montes, C., Valencia, V., Vanegas, J., Bustamante, C., Echeverri, S., 2018. The Paleogene arcs of the northern Andes of Colombia and Panama: insights on plate kinematic implications from new and existing geochemical, geochronological and isotopic data. Tectonophysics 749, 88–103.

Case, J.E., Duran S, L.G., Alfonso, L.R., Moore, W.R., 1971. Tectonic investigations in western Colombia and eastern Panama. Geol. Soc. Am. Bull. 82 (10), 2685–2712.

Castillo Manrique, A.F., 2018. Calculo de mecanismos focales a partir de eventos sísmicos en el Cluster de Murindó, Colombia. Undergraduate Thesis, Universidad de los Andes.

Chi, W.C., Dreger, D., Kaverina, A., 2001. Finite-source modeling of the 1999 Taiwan (Chi-Chi) earthquake derived from a dense strong-motion network. Bull. Seismol. Soc. Am. 91 (5), 1144–1157.

Cornthwaite, J., Bezada, M.J., Miao, W., Schmitz, M., Prieto, G.A., Dionicio, V., et al., 2021. Caribbean slab segmentation beneath northwest south America revealed by 3-D finite frequency teleseismic P-wave tomography. G-cubed 22 (4), e2020GC009431.

Cortés, M., Angelier, J., 2005. Current states of stress in the northern Andes as indicated by focal mechanisms of earthquakes. Tectonophysics 403 (1–4), 29–58.

Dionicio, V., Sánchez, J.J., 2012. Mapping of b-values, earthquake relocation, and Coulomb stress changes during 1992–2007 in the Murindó seismic zone, Colombia. J. Seismol. 16 (3), 375–387.

Duputel, Z., Rivera, L., Fukahata, Y., Kanamori, H., 2012. Uncertainty estimations for seismic source inversions. Geophys. J. Int. 190 (2), 1243–1256.

Duque-Caro, H., 1990. The Choco Block in the northwestern corner of South America: structural, tectonostratigraphic, and paleogeographic implications. J. S. Am. Earth Sci. 3 (1), 71–84.

Gómez, J., Montes, N.E., compiladores, 2020. Plancha 5-05 del Atlas Geológico de Colombia 2020. Servicio Geológico Colombiano, Bogotá. Escala 1:500 000.

Gómez, J., Montes, N.E., Nivia, A., Diederix, H., compiladores, 2015. Mapa Geológico de Colombia 2015. Servicio Geológico Colombiano, Bogotá. Escala 1:1 000 000.

Hartzell, S.H., Heaton, T.H., 1983. Inversion of strong ground motion and teleseismic waveform data for the fault rupture history of the 1979 Imperial Valley, California, earthquake. Bull. Seismol. Soc. Am. 73 (6A), 1553–1583.

Havskov, J., Ottemöller, L., 1999. SEISAN earthquake analysis software. Seismol Res. Lett. 70 (5), 532–534.

Heaton, T.H., 1990. Evidence for and implications of self-healing pulses of slip in earthquake rupture. Phys. Earth Planet. Interiors 64 (1), 1–20. https://doi.org/10.1016/0031-9201(90)90002-F.

Ide, S., 2007. Slip inversion. In: Treatise on Geophysics: Earthquake Seismology, vol. 4. Elsevier, pp. 193–222.

Julian, B.R., Miller, A.D., Foulger, G.R., 1998. Non-double-couple earthquakes 1. Theory. Rev. Geophys. 36 (4), 525–549.

Kennett, B.L., Engdahl, E.R., Buland, R., 1995. Constraints on seismic velocities in the Earth from traveltimes. Geophys. J. Int. 122 (1), 108–124.

Koulakov, I., 2009. LOTOS code for local earthquake tomographic inversion: benchmarks for testing tomographic algorithms. Bull. Seismol. Soc. Am. 99 (1), 194–214.

León, S., Cardona, A., Parra, M., Sobel, E.R., Jaramillo, J.S., Glodny, J., Valencia, V.A., Chew, D., Montes, C., Posada, G., Monsalve, G., Pardo-Trujillo, A., 2018. Transition from collisional to subduction-related regimes: an example from Neogene Panama-Nazca-South America interactions. Tectonics 37 (1), 119–139.

Li, Y., Toksöz, M.N., 1993. Study of the source process of the 1992 Colombia Ms= 7.3 earthquake with the empirical Green's function method. Geophys. Res. Lett. 20 (11), 1087–1090.

Lienert, B.R., Havskov, J., 1995. A computer program for locating earthquakes both locally and globally. Seismol Res. Lett. 66 (5), 26–36.

Lomax, A., Michelini, A., Curtis, A., 2009. Earthquake location, direct, global-search methods. In: Encyclopedia of Complexity and System Science, vol. 5. Springer, New York, pp. 2449–2473.

Melgar, D., Geng, J., Crowell, B.W., Haase, J.S., Bock, Y., Hammond, W.C., Allen, R.M., 2015. Seismogeodesy of the 2014 Mw6.1 Napa earthquake, California: rapid response and modeling of fast rupture on a dipping strike-slip fault. J. Geophys. Res. Solid Earth 120 (7), 5013–5033.

Montagner, J.P., Kennett, B.L.N., 1996. How to reconcile body-wave and normal-mode reference Earth models. Geophys. J. Int. 125 (1), 229–248.

Mora-Páez, H., Peláez-Gaviria, J.R., Diederix, H., Bohórquez-Orozco, O., Cardona-Piedrahita, L., Corchuelo-Cuervo, Y., Ramírez-Cadena, J., Díaz-Mila, F., 2018. Space geodesy infrastructure in Colombia for geodynamics research. Seismol Res. Lett. 89 (2A), 446–451.

Ojeda, A., Havskov, J., 2001. Crustal structure and local seismicity in Colombia. J. Seismol. 5 (4), 575–593.

Paris, G., Machette, M., Dart, R., Haller, K., 2000. Map and Database of Quaternary Faults and Folds in Colombia and its Offshore Regions. USGS. *Open File report. CO-0284*.

Podvin, P., Lecomte, I., 1991. Finite difference computation of traveltimes in very contrasted velocity models: a massively parallel approach and its associated tools. Geophys. J. Int. 105 (1), 271–284.

Restrepo, J.J., Toussaint, J.F., 1988. Terranes and continental accretion in the Colombian Andes. Episode. J. Int. Geosci. 11 (3), 189–193.

Snoke, J.A., Lee, W.H.K., Kanamori, H., Jennings, P.C., Kisslinger, C., 2003. FOCMEC: focal mechanism determinations. Int. Handbook Earthquake Eng. Seismol. 85, 1629–1630.

Sokos, E.N., Zahradnik, J., 2008. ISOLA a Fortran code and a Matlab GUI to perform multiple-point source inversion of seismic data. Comput. Geosci. 34 (8), 967–977.

Sokos, E., Zahradník, J., 2013. Evaluating centroid-moment-tensor uncertainty in the new version of ISOLA software. Seismol Res. Lett. 84 (4), 656–665.

Sun, M., Bezada, M.J., Cornthwaite, J., Prieto, G.A., Niu, F., Levander, A., 2022. Overlapping slabs: untangling subduction in NW South America through finite-frequency teleseismic tomography. Earth Planet Sci. Lett. 577, 117253.

Taboada, A., Rivera, L.A., Fuenzalida, A., Cisternas, A., Philip, H., Bijwaard, H., et al., 2000. Geodynamics of the northern Andes: subductions and intracontinental deformation (Colombia). Tectonics 19 (5), 787–813.

Vargas, C.A., 2020. Subduction geometries in northwestern South America. In: Gómez, J., Pinilla–Pachon, A.O. (Eds.), The Geology of Colombia, Volume 4 Quaternary, vol. 38. Servicio Geológico Colombiano, Publicaciones Geológicas Especiales, Bogotá, pp. 397–422.

Vargas, C.A., Mann, P., 2013. Tearing and breaking off of subducted slabs as the result of collision of the Panama arc indenter with northwestern South America. Bull. Seismol. Soc. Am. 103 (3), 2025–2046.
Vavryčuk, V., 2005. Focal mechanisms in anisotropic media. Geophys. J. Int. 161 (2), 334–346.
Zahradnik, J., Gallovic, F., Sokos, E., Serpetsidaki, A., Tselentis, A., 2008a. Quick fault-plane identification by a geometrical method: application to the Mw 6.2 Leonidio earthquake, 6 January 2008, Greece. Seismol Res. Lett. 79 (5), 653–662.
Zahradnik, J., Sokos, E., Tselentis, G.A., Martakis, N., 2008b. Non-double-couple mechanism of moderate earthquakes near Zakynthos, Greece, April 2006; explanation in terms of complexity. Geophys. Prospect. 56 (3), 341–356.
Zhu, L., Rivera, L.A., 2002. A note on the dynamic and static displacements from a point source in multilayered media. Geophys. J. Int. 148 (3), 619–627.